$(BZA)_2PbBr_4$
A potential scintillator for photon-counting computed tomography detectors

van Blaaderen, J. Jasper; van der Sar, Stefan; Onggo, Djulia; Sheikh, Md Abdul K.; Schaart, Dennis R.; Birowosuto, Muhammad D.; Dorenbos, Pieter

DOI
10.1016/j.jlumin.2023.120012

Publication date
2023

Document Version
Final published version

Published in
Journal of Luminescence

Journal of Luminescence 263 (2023) 120012

Contents lists available at ScienceDirect

Journal of Luminescence

journal homepage: www.elsevier.com/locate/jlumin

Full Length Article

$(BZA)_2PbBr_4$: A potential scintillator for photon-counting computed tomography detectors

J. Jasper van Blaaderen [a,*], Stefan van der Sar [a], Djulia Onggo [b], Md Abdul K. Sheikh [c], Dennis R. Schaart [a,d], Muhammad D. Birowosuto [c], Pieter Dorenbos [a]

[a] Delft University of Technology, Faculty of Applied Sciences, Department of Radiation Science and Technology, Mekelweg 15, 2629 JB Delft, Netherlands
[b] Inorganic and Physical Chemistry Research Group, Faculty of Mathematics and Natural Sciences, Institut Teknologi Bandung, Jl. Ganesha 10, Bandung 40132, Indonesia
[c] Łukasiewicz Research Network—PORT Polish Center for Technology Development, Stabłowicka 147, 54-066 Wrocław, Poland
[d] Holland Proton Therapy Center (HollandPTC), Huismansingel 4, 2629 JH Delft, the Netherlands

A B S T R A C T

Due to recent development in detector technology, photon-counting computed tomography (PCCT) has become a rapidly emerging medical imaging technology. Current PCCT systems rely on the direct conversion of X-ray photons into charge pulses, using CdTe, CZT, or Si semiconductor detectors. Indirect detection using ultrafast scintillators coupled to silicon photomultipliers (SiPM) offers a potentially more straightforward and cost-effective alternative. In this work a new 2D perovskite scintillator, benzylamonium lead bromide $(BZA)_2PbBr_4$, is experimentally characterised as function of temperature. The material exhibits a 4.2 ns decay time under X-ray excitation at room temperature and a light yield of 3700 photons/MeV. The simulation tool developed by Van der Sar et al. was used to model the pulse trains produced by a SiPM-based $(BZA)_2PbBr_4$ detector. The fast decay time of $(BZA)_2PbBr_4$ results in outstanding count-rate performance as well as very low statistical fluctuations in the simulated pulses. These features of $(BZA)_2PbBr_4$, combined with its cost-effective synthesis make $(BZA)_2PbBr_4$ very promising for PCCT.

1. Introduction

One of the most commonly used medical imaging techniques is X-ray computed tomography (CT). CT is nevertheless still limited by its spatial resolution, contrast-to-noise ratio for a given radiation dose, and artefacts [1,2]. New developments in photon-counting detector technology can help solve these problems. Such detectors must be able to handle the high flux used in CT [3,4]. Current detectors for photon-counting computed tomography (PCCT) are based on direct conversion of an X-ray photon's energy into charge, using either CdTe [5], CdZnTe (CZT) [6], or Si [7] semiconductors. For the first two materials however, availability and synthesis cost involved with producing low defect density materials are a bottleneck [1,2]. Si based detectors suffer from their low density ($\rho = 2.3$ g/cm^{-3}) and atomic number ($Z = 14$) [8]. Alternatively, PCCT detectors could be based on indirect detection, utilising an ultrafast scintillator to absorb the X-rays and convert their energy into scintillation photons. The later are detected and converted into an electrical pulse by for example a silicon photomultiplier (SiPM). Van der Sar et al. have explored this approach, both theoretically and experimentally [9,10]. $LaBr_3$:Ce was used as scintillator, due to its short decay time constant of 16 ns and high light yield of 63.000 photons/keV, and SiPMs as ultra fast photodetector. Hybrid Organic-Inorganic Perovskite (HOIP) scintillators, presented in this work, are another potential candidate for SiPM-based PCCT detectors.

HOIP's have become common materials for many optoelectronic applications in the past decade [11–13]. These materials have also gained interest in other fields, such as scintillation [14–17]. HOIP's differ from traditional scintilators, based on lanthanide activated materials [18–21], by being intrinsic scintillators. This allows for the use of small bandgap materials, significantly enhancing the theoretical light yield compared to traditional scintillators [22–24]. Especially two-dimensional perovskites are promising scintillator materials due to their stable room-temperature exciton luminescence [25,26].

Currently the best studied 2 dimensional perovskite scintillators are butylammonium lead bromide ($(BA)_2PbBr_4$) and phenethylammonium lead bromide ($(PEA)_2PbBr_4$) [14–16]. These two compounds are especially interesting due to their short decay times of 8.0 ns and 35 ns, respectively [14,16]. Combined with the possibility of cost-effective low temperature solution based synthesis, 2 dimensional perovskites are potential candidates to become the next generation scintillators [15,27].

* Corresponding author.
E-mail address: J.J.vanBlaaderen@tudelft.nl (J.J. van Blaaderen).

https://doi.org/10.1016/j.jlumin.2023.120012
Received 15 May 2023; Received in revised form 9 June 2023; Accepted 14 June 2023
Available online 16 June 2023

The short decay times of $(BA)_2PbBr_4$ and $(PEA)_2PbBr_4$ make them very interesting for high count rate applications such as PCCT [1]. Unfortunately, as demonstrated by Van der Sar et al., using $LaBr_3$:Ce, these decay times are still too slow for clinical PCCT applications.

In this work a new scintillator, benzylammonium lead bromide ($(BZA)_2PbBr_4$), is experimentally characterised as function of temperature. Currently, this material has only been studied at room temperature under UV-Vis excitation, showing a short decay time of approximately 3 ns, in addition to studies focusing on the crystal structure [28–31]. $(BZA)_2PbBr_4$ is a 2D perovskite very similar to $(PEA)_2PbBr_4$; the later contains two CH_2 groups in the spacer chain between the phenyl group and the NH_3 group while $(BZA)_2PbBr_4$ only contains one [31]. The goal of this work is to study $(BZA)_2PbBr_4$ under X-ray and γ-photon excitation and access its scintillation properties. The experimental results are used to simulate the performance of a $(BZA)_2PbBr_4$ and SiPM-based PCCT detector using the model developed by Van der Sar et al. [9,10]. The output of this simulation is compared with $(PEA)_2PbBr_4$, LYSO:Ce, $LaBr_3$:Ce and CZT in order to develop an understanding of the suitability of $(BZA)_2PbBr_4$ for use in SiPM-based PCCT detectors.

2. Results

Fig. 1a shows the pulse height spectrum of a $(BZA)_2PbBr_4$ crystal (6 mm x 4 mm x 0.5 mm) measured on a photomultiplier tube (PMT), using 662 keV gamma photons from ^{137}Cs. The rightmost peak is assigned to the total absorption of 662 keV photons, and is used to calibrate the spectrum. Due to the small thickness of the sample (0.5 mm) the probability of a characteristic Pb Kα X-ray to escape from the sample appears larger than 50%. This results in the more intense escape peak at 75 keV lower energy. From the total absorption peak the light yield is determined to be 3700 photons / MeV, based on the method described by De Haas and Dorenbos [32]. Both the total absorption and escape peak are fitted using a Gaussian function, see the insert of Fig. 1a. From the full width at half maximum of the fit the energy resolution was determined to be 8% at 662 keV.

The same sample was used to study the light output as function of the deposited energy using different gamma photon sources. The resulting non-proportionality curve is shown in Fig. 1b. Ideally, this curve is a horizontal line, represented by the dashed line in Fig. 1b. For $(BZA)_2PbBr_4$ the light yield increases at deposited energies below 662 keV. The maximum deviation is 6% with respect to the light yield at 662 keV. The lead K-shell absorption edge is located at 88 keV, corresponding to the same energy where a dip in the light yield is observed. Similar behaviour is observed in traditional scintillators [33,34].

The 300 K and 10 K photoluminescence excitation and emission spectra are shown in Fig. 2a. The 300 K excitation spectrum shows 3 distinct bands centred around 285 nm, 370 nm, and 424 nm. A similar excitation spectrum has been measured for $(PEA)_2PbBr_4$ assigning the three bands to absorption of the phenyl group, the transition to the conduction band, and the exciton absorption peak respectively [16]. At 10 K the band around 424 nm has shifted to 415 nm and decreased both in relative intensity and in peak width. The band around 370 nm shows a shoulder near 395 nm.

The 300 K emission spectrum contains two main emission bands centred around 415 nm and 440 nm. Additionally, a tail extending from 450 nm to 600 nm with a weak band around 490 nm is observed. At 10 K one emission peak is observed centred around 416 nm. Additionally, a broad emission extending from 450 nm to 650 nm with very low intensity is observed. Fig. 2b, shows the emission spectra from 300 K down to 10 K. The 415 nm emission shows almost no shift, whereas the 440 nm emission starts to blue shift upon cooling, merging with the 415 nm emission around 150 K. This behaviour is very similar to the temperature dependent photoluminescence of $(PEA)_2PbBr_4$ [16].

The temperature dependent X-ray excited emission spectra of $(BZA)_2PbBr_4$ are shown in Fig. 2c. Compared to the room temperature UV-Vis excited emission spectrum, in Fig. 2a, only one emission peak is present in the room temperature X-ray excited emission spectrum. The peak is located at 432 nm and has a tail extending to 600 nm, which is a very suitable wavelength range for SiPMs [35–37]. The insert in Fig. 2 shows that upon cooling the emission peak starts to blue shift. This stops at 150 K, corresponding to the same temperature at which the two emissions observed in the UV-Vis excited emission spectrum have merged. The presence of only one emission peak under X-ray excitation versus two emission peaks under UV-Vis excitation was also observed in $(PEA)_2PbBr_4$. Based on the experiments presented in our previous work on $(PEA)_2PbBr_4$ this is ascribed to self absorption [16]. X-rays penetrate deeper into the crystal compared to UV-Vis photons resulting in a larger degree of self absorption of the scintillation light.

The spectral intensity under UV-Vis excitation, both the total and contributions of the 415 nm and 440 nm peaks, are shown in Fig. 2d. The later also shows the total spectral intensity under X-ray excitation. Upon cooling down from room temperature the total intensity under UV-Vis excitation increases. Reaching its maximum at 175 K, before decreasing to 45% of the maximum intensity. The initial increase coincides with the observed merging of the 440 nm emission peak with the 415 nm emission peak, see Fig. 2b. The integrated intensity of the 415 nm and 440 nm emission peaks show opposite behaviour around this temperature. The intensity of the 440 nm peak reaches its minimum at 150 K, while the integrated intensity of the 415 nm peak reaches its maximum at this temperature. In contrast, the total spectral intensity under X-ray excitation first decreases, almost reaching zero at 150 K.

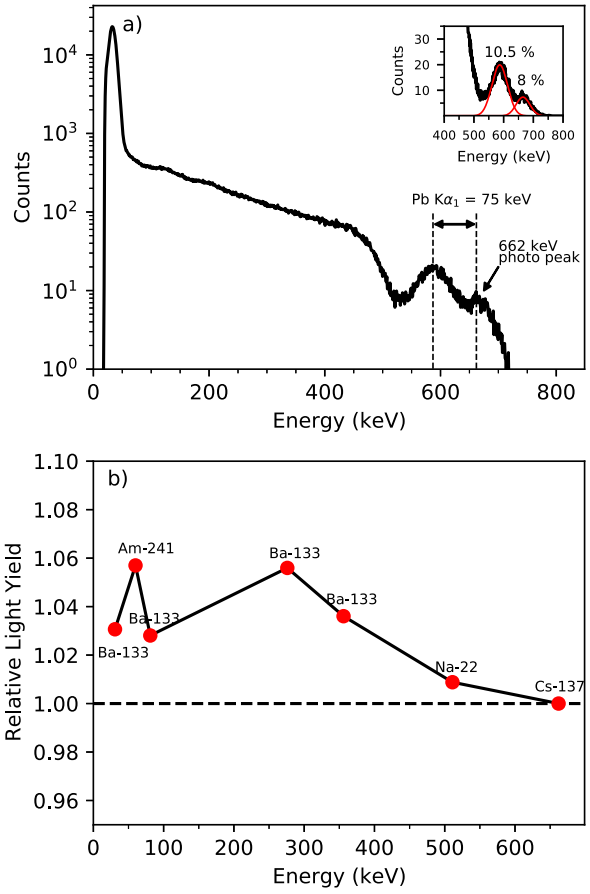

Fig. 1. (a) Pulse height spectrum of a $(BZA)_2PbBr_4$ crystal (6 mm x 4 mm x 0.5 mm) measured on a PMT, using a ^{137}Cs γ-source. In the plot both the total absorption and escape peak are indicated, based on their energy spacing. The insert shows both peaks fitted using a Gaussian function and their respective energy resolutions. (b) Non-proportional response of $(BZA)_2PbBr_4$, recorded using 662 keV from ^{137}Cs, 511 keV from ^{22}Na, 356 keV, 276 keV, 81 keV, 30.8 keV from ^{133}Ba, and 60 keV from ^{241}Am. The ideal response is indicated by the dashed horizontal black line.

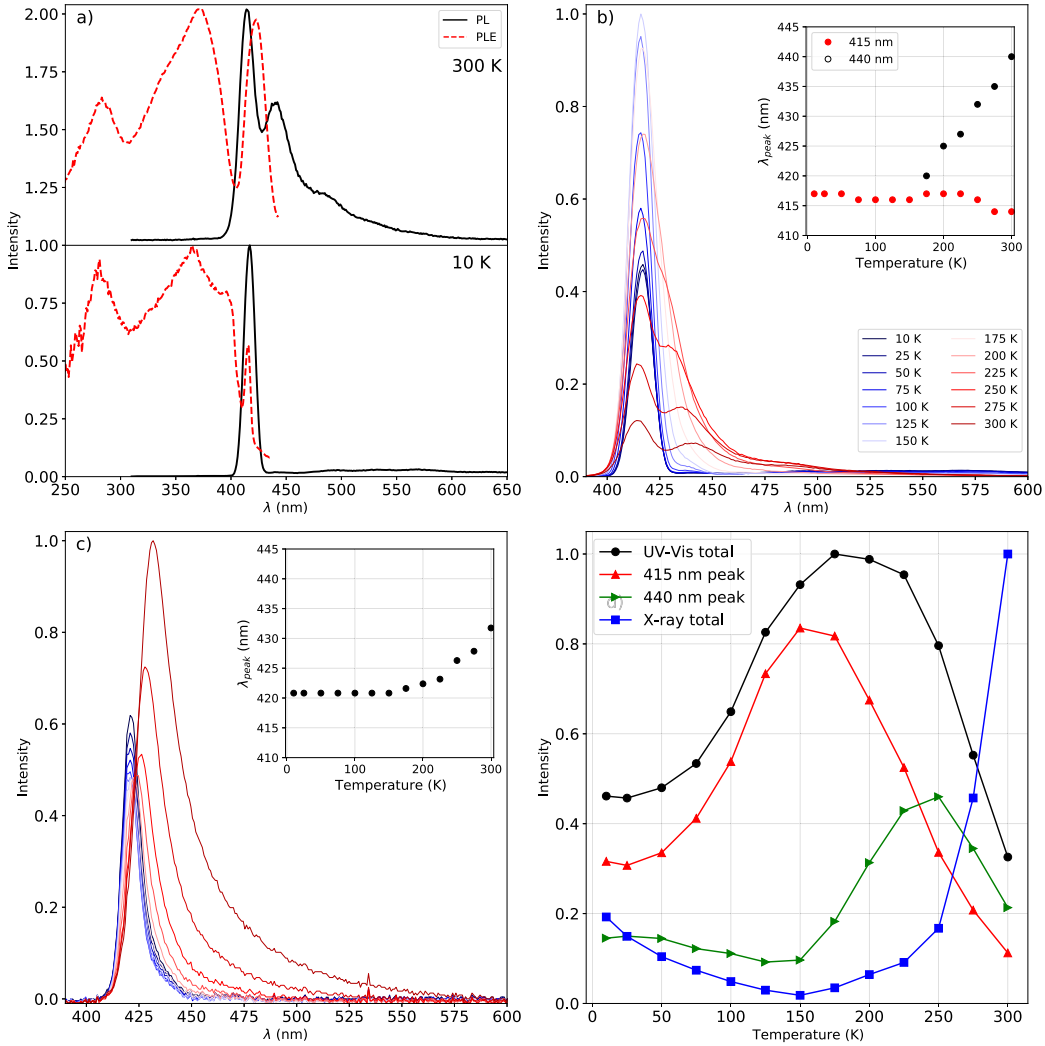

Fig. 2. (a) 300 K and 10 K photoluminescence emission (PL) (λ_{ex} = 280 nm) and excitation (PLE) (λ_{em} = 465 nm) spectra (b) Temperature dependent photoluminescence spectra (λ_{ex} = 280 nm) from 300 K down to 10 K. The legend applies for both (b) and (c). Insert: Peak position shift from 300 K down to 10 K of the 415 nm and 440 nm peaks. (c) X-ray excited emission spectra from 300 K down to 10 K. Insert: Peak position shift from 300 K down to 10 K. (d) Spectral intensity under UV-Vis, both the total and separate contributions of the 415 nm and 440 nm peaks, and X-ray excitation as function of temperature, from 300 K down to 10 K.

At this temperature the 432 nm emission stops blue shifting, reaching a wavelength of 420 nm, as can be observed in Fig. 2c. This behaviour of the total spectral intensity, both under UV-Vis and X-ray excitation, is similar to the behaviour observed for $(PEA)_2PbBr_4$ and $(BA)_2PbBr_4$ [14,16].

Fig. 3a shows the 300 K photoluminescence decay spectra of $(BZA)_2PbBr_4$ excited at 375 nm. The spectra are recorded in integral mode, monitoring all wavelengths, and at the peaks observed in Fig. 2a. The 1/e decay time, based on a single exponential model, for each decay spectrum is 3.3 ns which compares well with the average decay time constant of 3 ns reported by Dhanabalan et al. [28]. Fig. 3b shows a comparison between the photoluminescence decay spectra at 300 K and 20 K. At 20 K the decay time has increased significantly.

Fig. 3c shows the pulsed X-ray excited decay spectra measured from 300 K down to 13 K. The 300 K decay curve is slightly non-exponential, which disappears at 250 K. Below 100 K a fast decay component appears, with a decay time of 0.60 ns at 13 K. The decay times extracted from the decay curves, using either a single or bi-exponential model, are shown in Fig. 3d. The slow component observed at 13 K shows a linear decrease of its decay constant upon heating, reaching 4.2 ns at 300 K.

The combination of the 4.2 ns decay of $(BZA)_2PbBr_4$ under X-ray excitation and a reasonable light yield of 3700 photons/MeV makes this material very interesting for high count rate applications such as PCCT. To access the potential of $(BZA)_2PbBr_4$ for PCCT we used the simulation tool developed by Van der Sar et al. [9,10], which is based on a comprehensive model of the pulse trains produced by SiPM-based X-ray photon-counting scintillation detectors. Two metrics were defined to access the detector performance: A pulse duration metric t_{95} and a count rate capability metric r_{50} [9,10]. These metrics were calculated for $(BZA)_2PbBr_4$ using the properties reported in this work. For comparison, the properties of $(PEA)_2PbBr_4$ reported in our previous work [16], and literature values for LYSO:Ce, $LaBr_3$:Ce and CZT were used to calculate the same metrics. For the SiPM the following properties were used: photodetection efficiency = 0.28, recharge time constant = 7.0 ns, and optical crosstalk parameter = 0.1235. [9]. This combined with a light collection efficiency of 0.75 is used as input for the model [9].

The results of the simulation are summarised in Table 1. For $(BZA)_2PbBr_4$ we found t_{95} = 26 ns and r_{50} = 26.7 Mcps/pixel. Comparison with the other values in Table 1 shows that $(BZA)_2PbBr_4$ performs not only better than LYSO:Ce and $LaBr_3$:Ce but also better than CdTe/CZT.

Furthermore, the level of statistical fluctuations on the raw pulses of a $(BZA)_2PbBr_4$ based detector, simulated examples are shown in Fig. 4, are very low compared to the fluctuations on pulses from of LYSO:Ce and $LaBr_3$:Ce based detectors [9]. This is caused by the fast decay of

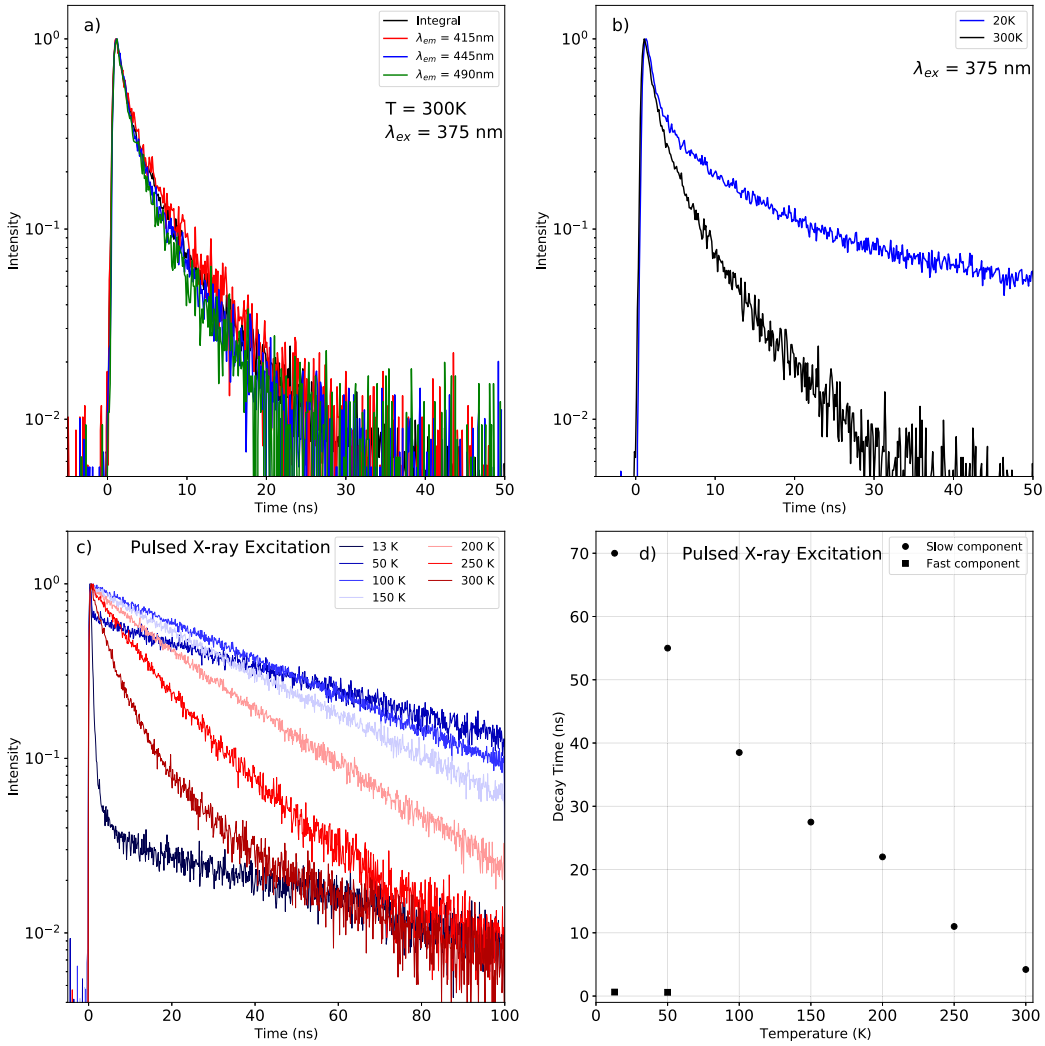

Fig. 3. (a) Room temperature time resolved photoluminescence spectra measured in integral mode, monitoring all wavelengths at the same time, and at wavelengths of 415 nm, 445 nm, and 490 nm. (b) 20 K and room temperature time resolved photoluminescence spectra, measured in integral mode. (c) Temperature dependent pulsed X-ray excited decay spectra from 300 K down to 13 K. (d) Temperature dependent change of the decay time constants obtained from the pulsed X-ray excited decay spectra.

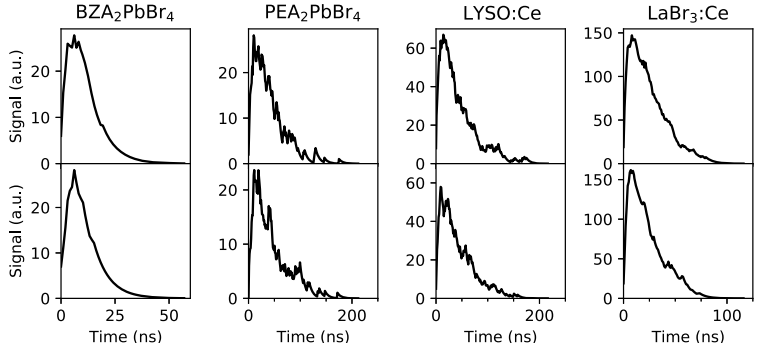

Fig. 4. Examples of simulated pulses for $(BZA)_2PbBr_4$, $(PEA)_2PbBr_4$, LYSO:Ce, and $LaBr_3$:Ce.

$(BZA)_2PbBr_4$ (4.2 ns), which is in fact faster than the SiPM response (7 ns). Hence, the pulse shapes are dominated by the deterministic SiPM response rather than the statistical response of the scintillator. As such, the negative effect of the moderate light yield (3.7 photons/keV) on the scintillators response doesn't manifest, and hardly any low-pass filtering, which would result in unfavourable pulse elongation, is needed to obtain useful pulses.

3. Conclusion

The potential use of $(BZA)_2PbBr_4$ in a PCCT detector has been assessed based on the presented characterisation. An energy resolution of 8% and light yield of 3.7 photons/keV, both at 662 keV, have been measured. Additionally, the non-proportionality of the response of $(BZA)_2PbBr_4$ has been studied showing a maximum deviation of 6%

Table 1
Summary and comparison of physical, scintillation, and detection properties. Both emission wavelength and decay time are based on X-ray excited measurements. * 60 keV is just below the K-edge of Lu.

	$(BZA)_2PbBr_4$	$(PEA)_2PbBr_4$	LYSO:Ce	$LaBr_3$:Ce	CZT
Detection Method	Indirect	Indirect	Indirect	Indirect	Direct
Hygroscopic	No	No	No	Yes	No
Production Methods	Solution	Solution	Czochralski	Bridgman	Bridgman
Max Emission Wavelength (nm)	432	440 [16]	420 [38]	380 [38]	
Decay Time (ns)	4.2	35.2 [16]	36 [38]	16 [38]	
Density (g/cm^3)	2.23 [31]	2.26 [31]	7.1 [38]	5.08 [38]	5.78
Light Yield @ 662 keV (photons/keV)	3.7	11 [14]	33 [38]	63 [38]	
Energy Resolution @ 662 keV	8%	10% [14]	8% [38]	2.6% [38]	0.6% [39]
Linear attenuation length @ 60 keV (cm^{-1})	5.8	5.8	19*	25.8	36
Pulse Duration t_{95} (ns) [9]	26	109	112 [9]	57 [9]	34 [9]
Count Rate Capability r_{50} (Mcps/pixel) [9]	26.7	6.4	6.2 [9]	12.2 [9]	20.4 [9]

at 60 keV. At room temperature a single emission peak at 432 nm is observed under X-ray excitation, while under UV-Vis excitation two emission peaks, 415 nm and 440 nm, are observed. This difference is ascribed to self absorption. The total spectral intensity decreases significantly at lower temperatures. At room temperature an X-ray excited decay time of 4.2 ns has been measured.

Due to this fast decay time the potential X-ray count-rate performance of $(BZA)_2PbBr_4$ is outstanding, with predicted values of t_{95} and r_{50} of 26 ns and 26.7 Mcps/pixel respectively, outperforming state-of-the-art CdTe/CZT detectors. The simulated pulses showed little statistical fluctuations due to the fact that the 4.2 ns decay of $(BZA)_2PbBr_4$ is faster than the SiPM response of 7 ns. These features of $(BZA)_2PbBr_4$, combined with its cost-effective synthesis, which is still a major concern for detector-grade CdTe/CZT, make $(BZA)_2PbBr_4$ very promising for PCCT. The further development of the growth process of $(BZA)_2PbBr_4$ could improve its light yield and energy resolution, making this material even more interesting.

4. Experimental

$(BZA)_2PbBr_4$ crystals were synthesised by dissolving $PbBr_2$ (0.73 g, ≥ 98% Merck) in HBr (5 ml, 48% aqueous Merck) until a clear solution was formed. To this solution $C_6H_5CH_2NH_2$ (0.7 ml, ≥ 98% Merck) was added, immediately forming a white suspension. To this suspension 35 ml deionised water was added. The mixture was stirred vigorously and warmed at 100 °C for 1 hour to achieve a homogeneous clear solution. Crystals started to form when the mixture was left overnight at room temperature. The crystals were separated from the solution after two days and dried in aeration. This resulted in a product yield of 45% (0.48 g). The crystal structure was determined using XRD and matches the structures presented in literature well [31].

The presented photoluminescence emission and excitation spectra were measured using a 450 W Xenon lamp. The light first passes through a Horiba Gemini 180 monochromater before hitting the sample. Afterwards the emitted light passes through a Princeton Instruments SpectraPro-SP2358 monochromater on which a Hamamatsu R7600U-20 PMT is attached. All spectra are corrected for the lamp intensity. The samples were mounted on a closed cycle helium cryostat operating below 10^{-4} mbar.

The presented X-ray excited emission spectra were recorded by exciting the sample using X-rays from an tungsten anode X-ray tube operating at 79 kV, with an average energy of 40 keV. The low energy side of the produced X-ray spectrum is filtered out of the X-ray beam to prevent radiation damage. The samples were mounted on a closed cycle helium cryostat operating below 10^{-4} mbar. The emitted light is detected by an Ocean Insights QE Pro Spectrometer.

The presented time resolved photoluminescence spectra are measured via the time-correlated single photon counting methods. A PicoQuant LDH-P-C-375M pulsed diode laser excites the sample. The laser is triggered by a PicoQuant laser driver, whose reference output functions as the start signal and is connected to an Ortec 567 time-to-amplitude converter (TAC). An Ortec 462 time calibrator is used to calibrate the bin width. The emitted light passes through a Princeton Instruments VM-504 monochromator and is detected by an ID Quantique id100-50 single-photon counter. The signal is digitised by an Ortec AD144 amplitude to digital converter. The samples were mounted on a closed cycle helium cryostat operating below 10^{-4} mbar.

The presented X-ray excited decay spectra are measured via the time-correlated single photon counting method using a Start:Stop ratio of approximately 5000:1 respectively. A PicoQuant LDH-P-C-440M pulsed diode laser is used to generate X-ray pulses from a Hamamatsu N5084 light excited X-ray tube, with an average energy of 18.2 keV. The laser is triggered by a PicoQuant laser driver, whose reference output functions as the start signal and is connected to an Ortec 567 time-to-amplitude converter (TAC). An Ortec 462 time calibrator is used to calibrate the bin width. An ID Quantique id100-50 single-photon counter was used to detect the emitted photons and functions as the stop signal. The signal first goes through a LeCroy 623B Octal Discriminator and analogue delay. The time differences are digitised using an Ortec AD114 amplitude to digital converter. The samples were mounted on a closed cycle helium cryostat operating below 10^{-4} mbar.

Pulse height spectra are recorded by placing the samples on a Hamamatsu R1791 PMT and covering them with PTFE tape. The PMT operates at -700 V. The signal first passes through an integrated preamplifier after which it is further processed by an Ortec 672 spectroscopic amplifier and digitized by an Ortec AD144 26 K ADC. All measurements were performed without optical coupling using a shaping time of 0.5 μs.

CRediT authorship contribution statement

J. Jasper van Blaaderen: Data curation, Formal analysis, Investigation, Visualization, Writing – original draft, Writing – review & editing. **Stefan van der Sar:** Formal analysis, Writing – review & editing. **Djulia Onggo:** Supervision, Writing – review & editing. **Md Abdul K. Sheikh:** Supervision, Writing – review & editing. **Dennis R. Schaart:** Formal analysis, Supervision. **Muhammad D. Birowosuto:** Supervision, Writing – review & editing. **Pieter Dorenbos:** Data curation, Formal analysis, Supervision, Writing – review & editing.

Declaration of competing interest

The authors declare that they have no known competing financial interests or personal relationships that could have appeared to influence the work reported in this paper.

Data availability

Data will be made available on request.

Acknowledgements

The authors acknowledge financial supports from the TTW/OTP grant no. 18040 of the Dutch Research Council. The authors would like to thank Arramel for his assistance in the crystal growth process.

References

[1] T. Flohr, M. Petersilka, A. Henning, S. Ulzheimer, J. Freda, B. Schmidt, Phys. Med. 79 (2020) 126–136, https://doi.org/10.1016/j.ejmp.2020.10.030.
[2] U.N. Roy, G.S. Camarda, Y. Cui, R. Gul, A. Hossain, G. Yang, J. Zazvorka, V. Dedic, J. Franc, R.B. James, Sci. Rep. 9 (2019) 1620, https://doi.org/10.1038/s41598-018-38188-w.
[3] S.S. Hsieh, S. Leng, K. Rajendran, S. Tao, C.H. McCollough, IEEE Trans. Radiat. Plasma Med. Sci. 5 (2021) 441–452, https://doi.org/10.1109/TRPMS.2020.3020212.
[4] M. Persson, R. Bujila, P. Nowik, H. Andersson, L. Kull, J. Andersson, H. Bornefalk, M. Danielsson, Med. Phys. 43 (2016) 4398–4411, https://doi.org/10.1118/1.4954008.
[5] S. Kappler, A. Henning, B. Kreisler, F. Schoeck, K. Stierstorfer, T. Flohr, Proceedings Volume 9033, Medical Imaging 2014: Physics of Medical Imaging, 90331C, https://doi.org/10.1117/12.2043511.
[6] R. Steadman, C. Herrmann, A. Livne, Nucl. Instrum. Methods Phys. Res., Sect. A, Accel. Spectrom. Detect. Assoc. Equip. 862 (2017) 18–24, https://doi.org/10.1016/j.nima.2017.05.010.
[7] J. Da Silva, F. Gronberg, B. Cederstrom, M. Persson, M. Sjolin, Z. Alagic, R. Buijla, M. Danielsson, J. Med. Imag. 6 (2019) 043502, https://doi.org/10.1117/1.JMI.6.4.043502.
[8] M. Danielsson, M. Persson, M. Sjolin, Phys. Med. Biol. 66 (2021) 03TR01, https://doi.org/10.1088/1361-6560/abc5a5.
[9] S.J. van der Sar, S.E. Brunner, D.R. Schaart, Med. Phys. 48 (2021) 6324–6338, https://doi.org/10.1002/mp.14886.
[10] S.J. van der Sar, D. Leibold, S.E. Brunner, D.R. Schaart, in: Proceedings, 7th International conference on Image Formation in X-ray Computed Tomography, vol. 12304, 2022, 12304A.
[11] M.A. Green, A. Ho-Naillie, H.J. snaith, Nat. Photonics 8 (2014) 506, https://doi.org/10.1038/nphoton.2014.134.
[12] X.Y. Chin, D. Cortecchia, J. Yin, A. Bruno, C. Soci, Nat. Commun. 6 (2015) 7383, https://doi.org/10.1038/ncomms8383.
[13] L. Dou, Y.M. Yang, J. You, Z. Hong, W.-H. Chang, G. Li, Y. Yang, Nat. Commun. 5 (2014) 5404, https://doi.org/10.1038/ncomms6404.
[14] F. Maddalena, A. Xie Arramel, M.E. Witkowski, M. Makowski, B. Mahler, W. Drozdowski, T. Mariyappan, S.V. Springham, P. Coquet, C. Dujardin, M.D. Birowosuto, C. Dang, J. Mater. Chem. C 9 (2021) 2504, https://doi.org/10.1039/D0TC05647B.
[15] A. Xie, F. Maddalena, M.E. Witkowski, M. Makowski, B. Mahler, W. Drozdowski, S.V. Springham, P. Coquet, C. Dujardin, M.D. Birowosuto, C. Dong, Chem. Mater. 32 (2020) 8530–8539, https://doi.org/10.1021/acs.chemmater.0c02789.
[16] J.J. van Blaaderen, F. Maddalena, C. Dong, M.D. Birowosuto, P. Dorenbos, J. Mater. Chem. C 10 (2022) 11598–11606, https://doi.org/10.1039/D2TC01483A.
[17] L.J. Diguna, L. Jonathan, M.H. Mahyuddin Arramel, F. Maddalena, I. Mulyani, D. Onggo, A. Bachiri, M.E. Witkowski, M. Makowski, D. Kowal, W. Drozdowski, M.D. Birowosuto, Mater. Adv. 3 (2022) 5087–5095, https://doi.org/10.1039/D2MA00258B.
[18] E.V.D. van Loef, P. Dorenbos, C.W.E. van Eijk, Appl. Phys. Lett. 79 (2001) 1573, https://doi.org/10.1063/1.1385342.
[19] P. Dorenbos, Opt. Mater. X 1 (2019) 100021, https://doi.org/10.1016/j.omx.2019.100021.
[20] C. van Aarle, K.W. Kramer, P. Dorenbos, J. Lumin. 238 (2021) 11857, https://doi.org/10.1016/j.jlumin.2021.118257.
[21] C. van Aarle, K.W. Kramer, P. Dorenbos, J. Lumin. 251 (2022) 119209, https://doi.org/10.1016/j.jlumin.2022.119209.
[22] P. Dorenbos, IEEE Trans. Nucl. Sci. 57 (2010) 3, https://doi.org/10.1109/TNS.2009.2031140.
[23] M.D. Bitowosuto, D. Cortecchia, W. Drozdowski, K. Brylew, W. Lachmanski, A. Bruno, C. Soci, Sci. Rep. 6 (2016) 37254, https://doi.org/10.1038/srep37254.
[24] V.B. Mykhaylyk, H. Kraus, V. Kapustianyk, H.J. Kim, P. Mercere, M. Rudko, P. Da Silva, O. Antonyak, M. Dendebera, Sci. Rep. 10 (2020) 8601, https://doi.org/10.1038/s41598-020-65672-z.
[25] W.W. Wolszczak, D.L. Carrroll, R.T. Williams, Advanced X-ray detector technologies, Chapter 1, https://doi.org/10.1007/978-3-030-64279-2_1, 2022.
[26] R.T. Williams, W.W. Wolszczak, X. Yan, D.L. Carrol, ACS Nano 14 (2020) 5161–5169, https://doi.org/10.1021/acsnano.0c02529.
[27] F. Maddalena, L. Tjahjana, A. Xie Arramel, S. Zeng, H. Wang, P. Coquet, W. Drozdowski, C. Dujardin, C. Dang, M.D. Birowosuto, Crystals 9 (2019) 88, https://doi.org/10.3390/cryst9020088.
[28] B. Dhanabalan, A. Castelli, M. Palei, D. Spirito, L. Manna, R. Krahne, M. Arciniegas, Nanoscale 11 (2019) 8334–8342, https://doi.org/10.1039/C9NR00638A.
[29] B. Dhanabalan, A. Castelli, L. Ceseracciu, D. Spirito, F. Di Stasio, L. Manna, R. Krahne, M.P. Arciniegas, Nanoscale 13 (2021), https://doi.org/10.1039/D0NR08043H, 3948, 3956.
[30] Z. Yuan, Y. Shy, Y. Tian, Y. Xin, B. Ma, Chem. Commun. 51 (2015) 16385–16388, https://doi.org/10.1039/C5CC06750B.
[31] N. Kawano, M. Koshimizu, Y. Sun, N. Yahaba, Y. Fujimoto, T. Yanagida, K. Asai, J. Phys. Chem. C 118 (2014) 9101–9106, https://doi.org/10.1021/jp4114305.
[32] J.T.M. De Haas, P. Dorenbos, IEEE Trans. Nucl. Sci. 53 (2008) 3, https://doi.org/10.1109/TNS.2008.922819.
[33] P. Dorenbos, J.T.M. de Haas, C.W.E. van Eijk, IEEE Trans. Nucl. Sci. 42 (1995) 2190–2202, https://doi.org/10.1109/23.489415.
[34] I.V. Khodyuk, P. Dorenbos, IEEE Trans. Nucl. Sci. 59 (2012) 3320–3331, https://doi.org/10.1109/TNS.2012.2221094.
[35] W. Wolszczak, K.W. Krämer, P. Dorenbos, Phys. Status Solidi RRL 13 (2019) 1900158, https://doi.org/10.1002/pssr.201900158.
[36] C. Piemonte, A. Gola, Nucl. Instrum. Methods Phys. Res., Sect. A, Accel. Spectrom. Detect. Assoc. Equip. 926 (2019) 2–15, https://doi.org/10.1016/j.nima.2018.11.119.
[37] Y. Haemisch, T. Frach, C. Degenhardt, A. Thon, Phys. Proc. 37 (2012) 1546–1560, https://doi.org/10.1016/j.phpro.2012.03.749.
[38] Datas Sheet Luxium solutions, obtained January 2023, https://www.crystals.saint-gobain.com/radiation-detection-scintillators/crystal-scintillators.
[39] F. Zhang, C. Herman, Z. He, G. De Geronimo, E. Vernon, J. Fried, IEEE Trans. Nucl. Sci. 59 (2012) 236–242, https://doi.org/10.1109/TNS.2011.2175948.